| | |
|---|---|
| ***Publication Year*** | 2018 |
| ***Acceptance in OA@INAF*** | 2021-01-29T09:39:50Z |
| ***Title*** | Lynx optics based on full monolithic shells: design and development |
| ***Authors*** | CIVITANI, Marta Maria; VECCHI, Gabriele; Holyszko, J.; Basso, S.; Ghigo, M.; et al. |
| ***DOI*** | 10.1117/12.2313541 |
| ***Handle*** | http://hdl.handle.net/20.500.12386/30098 |
| ***Series*** | PROCEEDINGS OF SPIE |
| ***Number*** | 10699 |

# Lynx optics based on full monolithic shells: design and development

Civitani, M., Vecchi, G., Holyszko, J., Basso, S., Ghigo, M., et al.

M. Civitani, G. Vecchi, J. Holyszko, S. Basso, M. Ghigo, G. Pareschi, G. Parodi, G. Toso, K. Kiranmayee, J. Davis, R. Elsner, D. Swartz, "Lynx optics based on full monolithic shells: design and development," Proc. SPIE 10699, Space Telescopes and Instrumentation 2018: Ultraviolet to Gamma Ray, 1069911 (5 October 2018); doi: 10.1117/12.2313541

Event: SPIE Astronomical Telescopes + Instrumentation, 2018, Austin, Texas, United States

# Lynx X-ray optics based on thin full monolithic shells: Design and development

M. Civitani[a1], G. Vecchi[a], J. Hołysko[a], S. Basso[a], M. Ghigo[a], G. Pareschi[a],
G. Parodi[c], G. Toso[b] , K. Kiranmayee[d] , J. Davis[d], R. Elsner[d] , D. Swartz[d]

[a]INAF-OAB, Via E. Bianchi 46, 23807 Merate (LC), Italy
[b]INAF-IASF, Via E. Bassini 15, 20133 Milano, Italy
[c]BCV Progetti, Via S. Orsola 1, 20123 Milano, Italy
[d]MSFC/USRA

## ABSTRACT

Lynx is the future X-ray Observatory with superb imaging capabilities (< 1 arcsec Half Energy Width, HEW) and large throughput (2 $m^2$ effective area @ 1 keV) being considered in US to take over Chandra. The implementation of the X-ray mirror module represents a very challenging aspect and different approaches are being considered. Thin and low-weight substrates, working in grazing incidence configuration, are necessary to meet the severe mass constraints but they have also to preserve the requirement of an excellent angular resolution. The use of monolithic glass (fused silica) shells is an attractive solution, provided that their thickness is maintained very small (<4 mm for mirror shells up of 3 m diameter). In this paper we present the opto-mechanical design of the Lynx mirror assembly based on this approach, together with the on-going technological development process. In particular, we discuss the figuring process, which is based on direct polishing followed by an ion beam figuring correction. A temporary structure is specifically devoted to support the shell during the figuring and polishing operations and to manage the handling of the shell through all phases up to integration into the final telescope supporting spoke wheel. The results achieved so far on a prototypal shell will be discussed.

**Keywords:** X-ray telescopes, X-ray mirrors, thin mirror shells, full shell, monolithic shells, fused silica, super polishing, Bonnet polishing, ion beam figuring, 3M™ Trizact™ , opto-mechanical mounts

## 1. INTRODUCTION

The *Lynx* design is based on an X-ray telescope with an unprecedented combination of superb angular resolution, wide FOV and large effective area [1,2]. The *Lynx* Mirror Assembly (LMA) relies on grazing-incidence optics working in the 0.15 keV to 10 keV energy range. The LMA focal length is 10 m and the outer diameter of the LMA is 3-m, allowing for maximum flexibility in the choice of launch vehicle and fairing size. The LMA requirements are summarized in Table 1.

The *Lynx* high-angular resolution requirement was established in the 1990's for the optics of the *Chandra* X- ray Observatory (formerly AXAF) [3]. *Chandra* is flying four full-shell mirror pairs with an exquisite angular resolution < 0.5 arcsec HEW, but providing a relatively modest effective area at 1 keV (~ 0.11 $m^2$). The mirrors were 1.6 - 2.4 cm thick mirrors made of Zerodur. They were fabricated combining a very accurate metrology and standard grinding and polishing techniques.

The *LMA* will require at least order of magnitude thinner mirror substrates without degrading the high angular resolution. As thin and lightweight mirrors are inherently not stiff, the extremely tight error margins will be a technical

---

[1] Corresponding author: marta.civitani@brera.inaf.it

Space Telescopes and Instrumentation 2018: Ultraviolet to Gamma Ray, edited by Jan-Willem A. den Herder,
Shouleh Nikzad, Kazuhiro Nakazawa, Proc. of SPIE Vol. 10699, 1069911 · © 2018 SPIE
CCC code: 0277-786X/18/$18 · doi: 10.1117/12.2313541

challenge, either during the production steps or for in-flight operation. In order to meet the *Lynx* requirements, multiple X-ray mirror technologies are under study:

- The adjustable segmented X-ray optics approach is based on piezo actuators deposited directly on the backside of slumped glass segments [4]. Furthermore, semiconductor strain gauges can be deposited directly on the piezoelectric cells. The strain can be correlated to local mirror bending and the calibration data used for on-orbit figure monitoring and correction.
- Lightweight mirrors can be realized using the grind-and-polish process on monocrystalline silicon segments [5]. Extremely thin flat silicon wafers are usually polished to highest figure and finish quality in the semiconductor industry. The silicon wafer manufacturing process has been adapted to making X-ray mirrors and a mounting concept based on meta-shell proposed.
- The 'full shell' concept [6] is based on the grinding, polishing, super polishing and final ion beam figuring correction of thin monolithic mirror shells. The shells are made of fused silica, a relatively cheap material but with adequate mechanical and thermal properties: low density (2.203 $g/cm^3$), low thermal expansion coefficient (0.5 x $10^{-6}$/K) and a good modulus of elasticity (70 GPa). The shells are very thin compared to the diameter: the thickness foreseen for a 3 m diameter shell is less than 4 mm. In this way it is possible to increase the number of the shells, and therefore the effective area, limiting the weight of the whole optics. The realization of these thin mirrors is possible taking advantage of the intrinsic stiffness of the monolithic axis-symmetric shells and adopting an ad hoc integration concept based on a Shell Supporting Structure (SSS) jig to be used for the handling and to support the shell in all the manufacturing steps.

In this paper we present the 'full shell' concept, discussing a preliminary opto-mechanical design of the mirror assembly (paragraph 2 and 3). The top-level error budget is discussed in paragraph 4, while the envisaged process is summarized in paragraph 5. The results of the test carried out on thin monolithic shells are summarized in paragraph 6, where the recent progress is the figuring of a section of a shell are described. The roadmap for the technology maturation program is reported in paragraph 7. Conclusions are stated in Paragraph 8.

**Table 1 – Requirements for the Lynx Mirror Assembly**

| Parameter | Requirement |
|---|---|
| HEW (On Axis) | 0.5 arcsec |
| Effective area (OnAxis, 1 keV) | > 2 $m^2$ |
| Field Of View Diameter | 20 arcmin |
| Grasp (HEW<1'', E=1keV) | > 600 $m^2$ * $arcmin^2$ |
| Maximum diameter | 3 m |
| Focal Length | 10 m |
| Mirror Module weight | 2000 kg (+ 500 kg margin) |

## 2. PRELIMINARY MIRROR MODULE MECHANICAL DESIGN

A preliminary evaluation of the Mirror Module (MM) structural behaviour has been carried out in the framework of a trade off between different assembly configurations. The detailed description of the optical design is given in Section 3, developed on the basis of the considerations of the present section. In this respect, three different configurations for the MM were analysed. They are represented in Figure 1. In the first and in the second case, the thin (a few mm) Mirror Shells (MS) are monolithic, with front and secondary surface directly joined at the intersection plane. In the first case, the MS are fixed at a Spoke Wheel (SW) at the top of the front surfaces, allowing the integration starting from innermost to outermost. In the second case, the MS are fixed at both ends to two spoke-wheels (positioned at the top and at the bottom). In the third case, the primary and secondary reflecting surfaces composing a MS (front and rear surfaces) are separated and fixed to a SW in the region of the intersection plane.

The three different proposed configurations assume similar reasonable resources (material, mass, spoke number, spoke wheel stiffness, etc.). The mechanical properties of the materials envisaged are reported in Table 2. Mirror shells are made of Fused Silica, a synthetic molten, high purity, non-crystalline quartz glass. The thermo-mechanical (T/M) properties of the material (in particular its low density and high Young modulus) are suitable to reach the necessary stiffness once that proper and optimized procedures are used. The Coefficient of Thermal Expansion (CTE) is very low, so that it can hold up very high thermal loads. Therefore, this material is very competitive with respect to Zerodur or ULE glasses, as the procurement cost of Fused Silica is lower. Iridium reflecting coating is assumed as a baseline. The connection of the MS to the SSS and to the MM structures is realized with an adhesive. Given that the SSS and the MM structure should match as much as possible the low CTE of Fused Silica, CFRP and INVAR are possible solutions for the the SSS and MM structures. Due to the high density of INVAR, the use of this material will be restricted to just mechanical couplings and components to be removed after the integration. In the current status, the mechanical properties of these materials are derived from literature and technical data sheets. The complete material characterization has to be done by proper future test campaigns.

As the strength depends on the surface conditions (surface damages, both on the front and back surface of the MS), a detailed characterization of the material properties allows the optimization of the process. The strength of the non-optical surfaces and of MS end sections could be increased with a proper surface treatment, for instance via chemical etching. Furthermore, the presence of stresses in the rough material has to be evaluated: the removal of stressed layers during MS grinding/polishing could give rise to spring back deformations during the final integration phase.

The configuration with the central SW turned out as the best choice for several reasons. It reduces the problems during MS manufacturing as there is no need of grinding and polishing the area between the primary and secondary surfaces in correspondence of the Intersection Plane (IP). Indeed, if the two surfaces are adjacent (as in Conf. 1 and 2), the accessibility is this area would be limited and a non-reflecting area, of at least some millimetres, should be envisaged. Moreover, with Conf. 3, the alignment of the two optical axes may be optimized during the integration phase and the best angular position can be precisely tuned in order to compensate the fabrication errors on the primary and the secondary surfaces. Finally, from the programmatic point of view, two separated surfaces allow the parallelization of the manufacturing process, which is particular important for larger shells. In this case, in fact, the grinding and polishing time are higher. Moreover, the MS have higher natural frequencies, given the shorter length. The mass distribution in the Mirror Module (MM) structure is better balanced, respect to the first configuration in Figure 1, with better performances in terms of frequencies and gravity load effects. In particular, this configuration is advantageous in lateral gravity condition, which is currently foreseen for on-ground calibration.

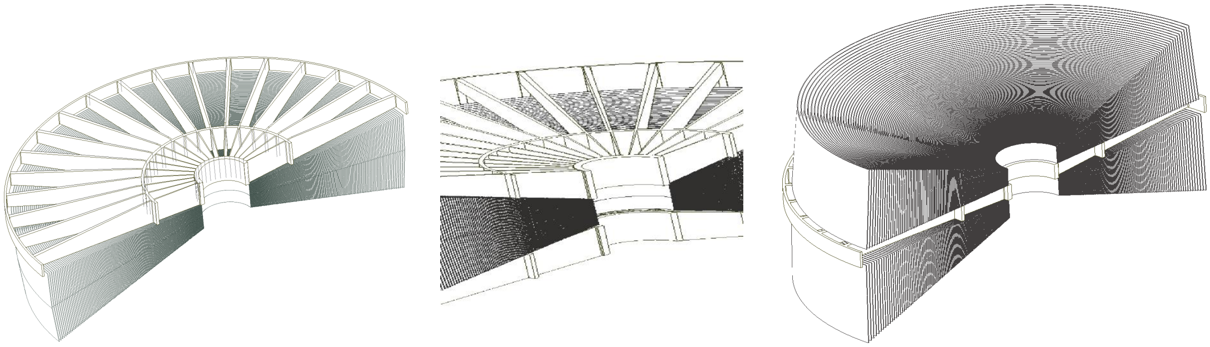

**Figure 1: Possible mirror assembly configurations considered for the trade-off. (#1) Single spoke wheel with short monolithic shell. (#2) Double spoke wheel. (#3) Single spoke between primary and secondary shells sections.**

**Table 2 – Mechanical properties of the materials, as derived from literature and technical data sheet. CFRP data represent just a preliminary rough assessment. The ΔCTE respect to $SiO_2$ and the stiffness could be improved by a proper CFRP design.**

| | $SiO_2$ | Ir | CFRP | Epoxy | Silicone RTV | INVAR 36 | INVAR 32-5 | Timetal 15-3 |
|---|---|---|---|---|---|---|---|---|
| **Young Modulus [GPa]** | 70 | 524 | 105 | 2.1 | 0.004 | 141 | 145 | 82 |
| **Poisson ratio** | 0.17 | 0.26 | 0.31 | 0.35^3) | 0.45 | 0.29 | 0.23 | 0.342 |
| **Density $t/m^3$]** | 2.201 | 22.65 | 1.73 | 1.2 | 1 | 8.05 | 8.14 | 4.78 |
| **CTE [$10^{-6}$ $K^{-1}$]** | 0.51 | 6.8 | 1.51 | 61 | 230 | 1.3 | 0.63 | 8.6 |
| **Uncured viscosity [cPs]** | NA | NA | NA | 225 / 425 | 3900 | NA | NA | NA |

The initial design of the SW foresees a bench with 7 radial partitions. The number of spokes increases with the radius. They have a solid rectangular cross section and their width is variable with the radius, so that 10% geometrical obscuration is obtained (see figure 3). The SW is made of CFRP, with a thickness in axial direction of 250 mm. As anticipated, in the current design, a conservative approach was used with respect to the CFRP mechanical properties. All the performances directly affected by the stiffness of MM structures will benefit by the improvement expected from the optimization of the composite material parameters.

With respect to the connections between the MS and the spokes, the preliminary results showed that proper connectors giving some radial decoupling between SW and MS are necessary. In this way, the thermal effects due to the materials CTE mismatch will be mitigated. Similar benefits apply also to gravity release effects and to stress peaks in MS at SW connections. On the other hand, the decoupling should be not too large to avoid spring back phenomena when MS constraints pass from SSS to the SW.

Gravity in axial or in lateral direction has been applied to the MM continuously supported in axial and tangent direction (radial free) at the outer ring. These loadings do not correspond to any effective configuration envisaged during the integration/testing process, but they are representatives of the intrinsic spoke wheel stiffness. The radial ($U_{R)}$ and axial ($U_A$) displacement contours related to axial and lateral gravity are reported respectively in figure 2 left panel and 2 centre panel. The impact of the reference temperature gradients has been analysed with kinematic constraints applied to the MM to allow thermal expansions. Three axial and three azimuthal rigid constraints, 120° spaced at outer ring, were assumed. Radial, lateral and bulk gradients were considered. $U_R$ and $U_A$ contours are shown in figure 2 right panel for a bulk gradient of 1°C.

The MS integration is foreseen to happen in vertical condition, with the gravity in axial direction and parallel to the optical axis. It will be carried out at as a "steady mass" process: the SW will be loaded by dummy masses to mimic the weight of the missing MSs. The dummy masses will be removed after the integration of each MS, so that the overall mass and the related SW deflections do not change along the whole process.

During the integration phase, an excessive elastic deflection of the SW should be avoided, as it degrades the performances of the LMA at the gravity release. A stiffer SW or a dedicated supporting scheme counteracts the axial gravity effects. A preliminary scheme based on astatic levers was considered: 12 astatic levers at the SW inner ring (1 m diameter) and 45 astatic levers + 3 axial / azimuthal supports 120° spaced at the outermost ring (3 m diameter). The SW drawing and the astatic levers scheme are shown in figure 3.

If the MM X-ray calibrations are carried out in the same configuration used during the integration (with axial gravity + supporting forces at work), in principle the gravity has no effect. On the contrary, the lateral gravity is disadvantageous condition in terms HEW degradation but the achieved results (HEW equal to 0.7 arcsec) are encouraging, as the optimization of the SW design and supporting system can improve the result further.

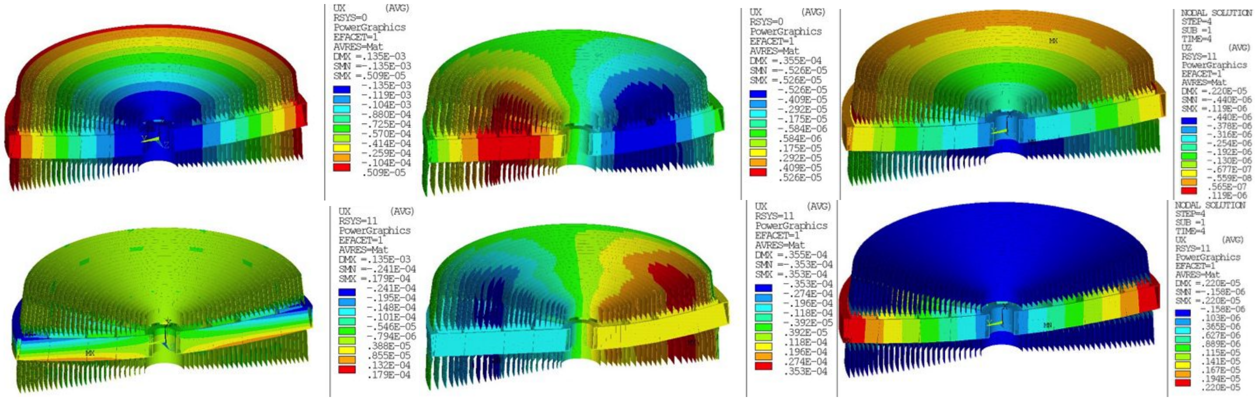

**Figure 2: From left to right: axial gravity, lateral gravity and $\Delta T = +1°C$ just on SW. $U_A$ contour (Top) $U_R$ contour (Bottom). Contours quoted in meters.**

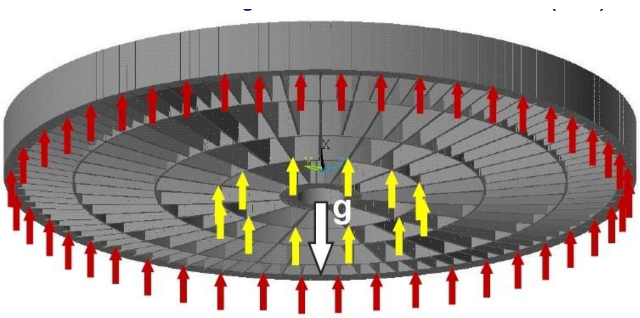

Figure 3: Supporting scheme during the integration phase.

The connections between MM and spacecraft structure were considered into two extreme ideal conditions: kinematic mounts at the outer ring (3 axial and tangential rigid constraints 120° spaced) or continuous (axial support + 3 tangent constraints 120° spaced at outer ring). The analysis has shown that it could be necessary providing at launch a certain number of provisional supports along the outer ring.

Gravity releases assessments refer to the integration procedure described before: a certain number of supporting forces are envisaged during the integration phase to mitigate the SW axial gravity deflections. In Figure 4 the axial and radial displacements of the SW at the gravity release are shown. The spoke wheel deformations, mitigated by proper MS-SW connectors, represent the major source of MS distortions.

Table 3 reports a summary of the ray-tracing results achieved in the different conditions. The MM was simulated by means of 14 “optical MS” radially distributed, having the real geometry, and 13 “dummy MS”. Each of these last ‘dummy MS’ is equivalent in terms of stiffness and mass to the whole MS set between two optical MS, so that they are representative of the whole MM. Just “optical MS” are used in the optical post processing of FEA. The mass of the SW was 348kg while the mass of the MS was 2081 kg, corresponding to a total mass of 2565 kg. The optical configuration used in these simulations was just slightly different from the one presented in the next Section 3. After this first assessment of the thermo-mechanical design, the optical design was then finalized. In order to limit the mass, the length and the position along the optical axis of the MS was adjusted and their thickness was reduced a little. Further, improvements in the structural performances are expected in future iterations between mechanical and optical design.

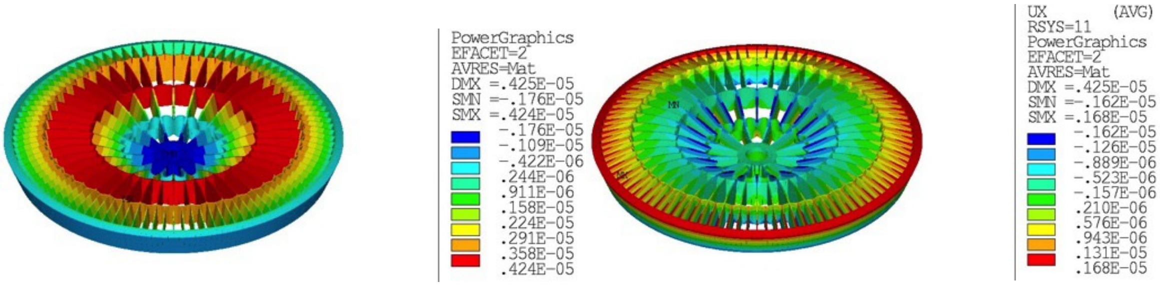

Figure 4: Axial displacements (Left) and radial displacements (Right) at gravity release. The range of spoke wheel displacement components is -1.8 / +4.2µm axial -1.6 / +1.7 µm radial.

Table 3 – Gravity, Reference temperature gradients and gravity release – MM ray tracing results. Results are given at Nominal Focus (NF) and at Best Focus (BF). ΔTU: uniform temperature change. TGA: axial thermal gradient. TGL: longitudinal thermal gradient. TGR: radial thermal gradient. ΔTS: temperature mismatch between ISW and MS.

| | **Gravity** | | **Thermal loading** | | | | | **Gravity release** |
|---|---|---|---|---|---|---|---|---|
| | **Axial** | **Lateral** | **ΔTU** | **TGA** | **TGL** | **TGR** | **ΔTS** | |
| **HEW$_{NF}$** [arcsec] | 1.17 | 2.00 | 0.26 | 0.06 | 0.55 | 0.20 | 0.37 | 0.38 |
| **90EW$_{NF}$** [arcsec] | 10.81 | 22.76 | 4.82 | 0.44 | 1.94 | 1.40 | 7.33 | 6.62 |
| **Δf** [mm] | -0.081 | - | +0.03 | -0.01 | - | -0.019 | +0.04 | -0.041 |
| **HEW$_{BF}$** [arcsec] | 1.01 | 2.00 | 0.15 | 0.03 | 0.55 | 0.20 | 0.22 | 0.26 |
| **90EW$_{BF}$** [arcsec] | 11.17 | 22.76 | 4.98 | 0.50 | 1.94 | 1.31 | 7.56 | 6.83 |

The MM frequencies were also computed assuming two extreme support conditions. In the first case, continuous radial and tangent supports at the outer SW ring are considered, while in the second case only three axial and three tangent supports at the outer SW ring were assumed. The results, achieved with rigid constrains, are reported in Table 4. On the basis of the final frequency requirement, a more realistic support condition (for instance usage of provisional supports at launch) will be defined.

The launch gives rise to severe loadings in terms of tensile stresses in the MS. Tensile stress peaks related to quasi-static loads at the SW interfaces are assessed in Table 5. A dedicated procedure was applied to avoid wrong and large peaks, erroneously generated by the application of point loads (nodal load) on the MS. Quasi static loading combinations were applied. The radial, the tangent and the axial forces at connectors between SW and MS were derived in four optical MSs These correspond to the largest MS (in terms of $\phi_{IP}$) respectively connected to 12/24/48/96 spokes. A detailed FEM of each MS in kinematic constraint conditions was implemented. SW interface reactions and quasi-static gravity loads were applied, so that loadings were self-balanced (null reaction forces at kinematic constraints). Each SW interface reaction force was spread on a square load-print 10mm×10mm. Tensile-stress peaks were computed on the detailed MS FEM. The SW bending deflections transmits radial displacements to the MS increasing the local bending stress in the shell. A further optimization of the SW stiffness is possible. The stress levels reported in Table 5 are demanding but are not prohibitive. Proper design optimization is needed to reduce stress level and risks on the basis of a reliable assessment of $SiO_2$ strength after the experimental campaigns.

**Table 4 – Continuous support & Kinematic mount – MM frequencies**

| | Continuous support | | Kinematic mount | |
|---|---|---|---|---|
| | **Frequency [Hz]** | **Effective mass [t]** | **Frequency [Hz]** | **Effective mass [t]** |
| Axial direction (X axis) | 35.4 | 2.00 (78%) | 54.3 | 1.77 (69%) |
| Lateral direction (Y axis) | 27.1<br>63.7 | 0.04 (1.4%)<br>1.26 (49%) | 93.3<br>97.8 | 0.74 (29%)<br>0.64 (25%) |
| Lateral direction (Z axis) | 27.1<br>63.7 | 0.04 (1.4%)<br>1.26 (49%) | 93.3<br>97.8 | 0.74 (29%)<br>0.64 (25%) |
| Rotation around X | 34.2 | 1.52 | 34.3<br>69.8 | 1.49<br>0.54 |
| Rotation around Y | 27.1 | 0.80 | 93.3 | 0.10 |
| Rotation around Z | 27.1 | 0.80 | 93.3 | 0.10 |

**Table 5 – MS stress peaks under load combinations [MPa]**

| MS #ID | $\phi_{IP}/2$ [mm] | Spoke number | Tensile stress peak [MPa] |
|---|---|---|---|
| 142 | 1472.2 | 96 | 5.35 |
| 119 | 1104.4 | 48 | 6.44 |
| 082 | 701.8 | 24 | 9.07 |
| 040 | 399.3 | 12 | 6.37 |

One of the drawback of the configuration with a central SW, is related to the larger number of end sections (four for each MS instead of 2). Given that each single component is shorter, the sensitivity to edge effects is larger. A typical edge effect is the tensioning of the coating. The simpler mitigation strategy will be the reduction of the coating stress. Some very promising results have been achieved by alternating different materials in the coating deposition [7]. In quasi-cylindrical geometries the tensioned coating effect is predictable. It mainly consists in edge effects, which damp toward the inner MS zone. So if a good coating homogeneity and repeatability is achieved (in terms of thickness and stress value), in principle it would be possible to correct the MS axial profile during grinding/polishing, to mitigate the elastic distortions induced by coating. The coating stress represents a problem for all technologies under investigation for the Lynx mission; indeed, closed and quasi-cylindrical MS are the less sensitive to such a problem.

## 3. OPTICAL DESIGN

Given the monolithic structure of the shells and the large diameter to account for, their thickness is a trade off between the mechanical requirements and optical performances. In order to limit the weight of the whole optics, the walls should be very thin compared to the diameter. This allows growing the number of the shells and therefore the effective area. On the other side too thin Mirror Shell (MS), being too floppy, encounters structural problems, making more severe all issues related to MS deformations.

Taking into account past evaluations, we started the preliminary design with thickness values sustainable from the mechanical point of view. The thickness foreseen for a 0.2 m diameter is 1.5 mm and increases linearly to 3.4 mm for a 3 m diameter shell. It is worth to note that optimization with respect to this choice can be made. In particular, better performances in terms of LMA total mirror mass can be achieved reducing the maximum thickness to lower values. Given the current partial knowledge of the material strength, this option could be chosen in a more advanced phase of the project, once a complete characterization of the glass will be carried out taking into account the surface finishing.

The preliminary optical design was generated taking into account the requirements reported in table 1. The LMA was designed in Wolter-Schwarzchild (WS) configuration [8], as it guarantees the best angular performances in the Field Of View (FOV).

From a general point of view, longer shells offer better area-to-mass ratio and concur to the reduction of the total number of shells to be realized. On the contrary, the requirement on the optical performances in the FOV introduces limitation into the geometrical configuration of the shells. The maximum length of the shell can be derived inverting the formula [8]:

$$\mathrm{HEW} = 1.34898 * 0.135*(xi+1)*((\tan(theta))^2/\tan(alfa))*(0.5*L/z0) \qquad (1)$$

With z0 = focal length, L = Length of the semi shell, xi =1, theta = Off axis angle at the edge of the FOV and alfa = ¼ *atan(r0/z0). It follows that the maximum MS length increases linearly with the radius. Given the limit in angular resolution at the edges of the FOV, the maximum height of the shell is fixed for each diameter. The larger shells can be longer, while the innermost one need to be shorter. The allowed maximum length, in dependence of the radius and the FOV limit, are reported in Figure 5. The values, corresponding to shells with radius 150 mm and 1500 mm, are reported in Table 6. The greater is the FOV, the shorter are the shells. Taking into account the limit at 1'' in the FOV and a 0.5'' margin to be distributed between the thermo mechanical, manufacturing and integration contributions, the HEW limit is set to 0.85'' at the edge of the FOV corresponding to lengths between 50.1 and 497.9 mm.

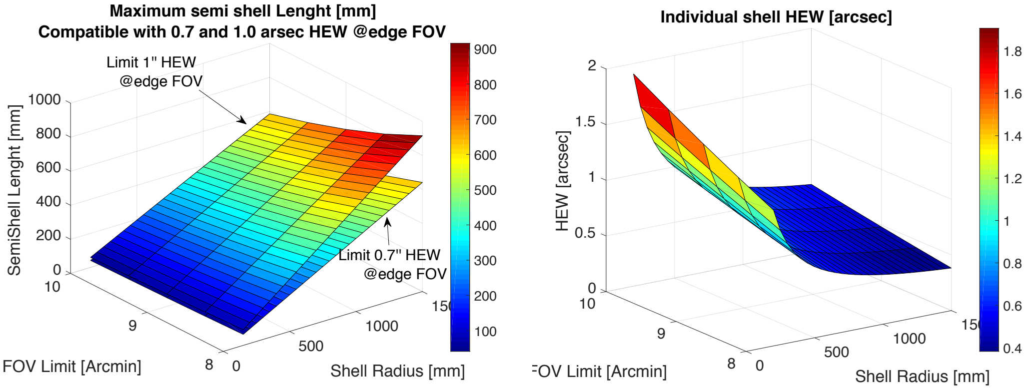

**Figure 5: (A) Maximum semi shell length allowed in order to respect the individual shell contribution of 1'' or 0.7'' for different values of the FOV. (B) HEW contribution in the FOV for the different shells in the selected geometrical configuration.**

The optical performances of the shells have been evaluated separately with a Ray-Tracing (RT). In figure 6 are shown the HEW on the best focal plane in dependence of the FOV for a Wolter-I (W1, black) and a WS (green) design. In yellow it is reported the expected behaviour inferred from the theoretical blurring equation. The results are given for shells with radius @IP equal to 200 mm and 1500 mm. Their lengths were fixed in accordance with the parameters derived from (1). Fixed the length, the improvement due to the WS design with respect to the standard Wolter-I is evident for large shells. For each of the cases, the bottom panel shows the position of the focal plane where the minimum HEW is found, in dependence from the off-axis photons arrival directions. The shells with smaller diameter present a focal plane with some millimetres of curvature. Instead, the outer shells have an almost flat focal plane. HEW values are compatible with the ones derived from the blurring formula. Therefore the ray-tracing software was judged suitable to derive the performances of the whole LMA presented in the next.

**Table 6 – Ranges of the semi shell length (radius @IP equal to 150 mm and 1500 mm)**

| | **Limit @ 8 '** | **Limit @ 9 '** | **Limit @ 10 '** |
|---|---|---|---|
| **HEW < 1.0''** | 92.2 – 915.3 mm | 72.8 – 723.2 mm | 59.0 - 585.8 mm |
| **HEW < 0.9 ''** | 82.9 -823.8 mm | 65.5 – 650.9 mm | 53.1 - 527.2 mm |
| **HEW < 0.8 ''** | 73.7 – 732.3 mm | 58.3 -578.6 mm | 47.2 - 468.6 mm |
| **HEW < 0.7''** | 64.5 - 640.7 mm | 51.0 – 506.3 mm | 41.3 – 410.1 mm |

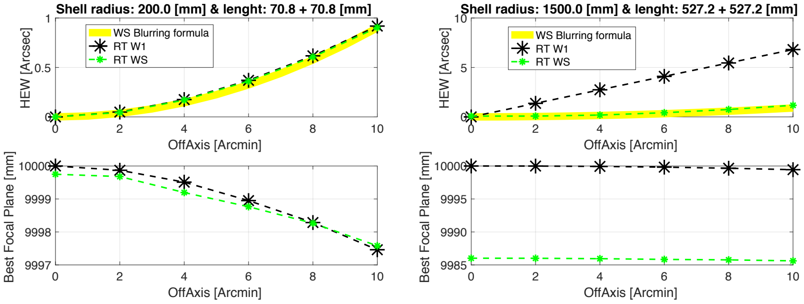

**Figure 6: HEW on the best focal plane in dependence of the FOV for a W1 (black) and a WS (green) design. In yellow it is reported the expected behaviour inferred from the theoretical blurring equation. For each of the cases, the bottom panel shows the position of the focal plane where the minimum HEW is found, in dependence from the off-axis photons arrival directions.**

With respect to the selection of innermost shell diameter, it is worth to note that the contribution to the effective area of the innermost shells is relevant only at high X-ray energy (>> 1 keV). With the current thickness selection (1.7 mm for 300 mm diameter), these shells are not really useful for increasing the effective area at low energy. On the other side, as they contribute to the requirement in the 6-8 keV, their geometry has been modified with respect to the WS prescription in order to improve their area to mass ratio. In particular, the minimum shell length is fixed to 150 mm, as the optical performances in the FOV of the innermost shells will be in any case limited, given the different curvature of their focal plane with respect to the larger shells. The optimization of the focal plane needs to be carried out taking into account of the collecting area contribution at low energies and therefore will follow the geometry required by larger shells. Moreover, given that the theoretical required length of the innermost shells is quite small (around 140 mm in total), longer shells will concur to overcome manufacturing problems.

**Table 7 – Main geometrical parameters for the shells of the preliminary optical design.**

| **Parameters** | **Values** |
|---|---|
| Gap @IP | 280 mm |
| Shift IP Inner/Outer | 2.3 - 124.7 mm |
| NumShellTot | 164 |
| R@IP Inner/Outer | 203.2 - 1483.8 mm |
| SemiShell height IP Inner/Outer | 157.9 - 348.2 mm |
| Thickness IP Inner/Outer | 1.6 – 3.4 mm |
| Weight IP Inner/Outer | 1.36 – 46.2 kg |
| Total mirror mass | 1890.7 kg |
| Mirror support structures & thermal control system | 300 kg (TBC) |

Further constrains have been fixed. The minimum diameter of the innermost shells has been fixed to 400 mm, with some margin on the accessibility with grinding and polishing existing equipments. Further reduction in the diameter may be taken into account with custom designed machines. In principle, the distance of innermost shells is a fraction of millimetre. It has been increased to 1 mm to allow a safety margin during the integration phase. This choice could be reduced in a more advanced project phase.

As explained in the former section, the optical design foresees detached primary and secondary mirror surface, integrated to form the complete LMA in a common spider structure. The connection with the LMA structure is realized only on one of the sides of the primary or secondary surface shell, in order to avoid over constrain. The primary mirror surface is integrated on the smaller diameter side, while the secondary surface is connected on the larger diameter. Taking into account a reasonable spider thickness and the fixation parts, a certain amount of free space between the primary and the secondary surface is left in the optical design. Taking into account the size of the optics, their weight and the preliminary mechanical design of the structure, the distance between the primary and the secondary mirror shells is set to 280 mm, constant for all the shells. Further optimizations could be evaluated in a more advanced phase. The main geometrical parameters of the 164 mirror shells, which compose the LMA, are listed in Table 7. The thickness ranges between 1.6 and 3.4 mm, while the length of the semi-shell is between 157.9 mm and 348.2. The weight of the shells ranges between 1.36 and 46.2 kg, with a total mirror mass of 1890.7 kg.

In accordance with WS design, the MS are distributed shifted along the optical axis on a spherical surface in order to satisfy the Abbe sine condition. The optical design started from the innermost shells adapting the focal length in order to guarantee the focal plane overlapping. The shift of the MS is maxima for outermost shells and it is around 125 mm. This curvature of the spider is advantageous from the structural point of view. Assuming a lightweight structure made of Silicon Carbide or CFRP the weight of the spider is estimated around 300 kg.

Two different reflecting coatings have been considered in the effective area evaluation. In the first case a layer of 40 nm Iridium ($\sigma = 0.5$ nm) is considered, while in the second a layer of Platinum with an over coating of Carbon (40 nm Pt + 10 nm C, $\sigma = 0.5$ nm) is assumed. The reflectivity up to 12 keV of the Ir and of the Pt + C is reported in Figure 7. At 1 keV, the Pt + C performs better than the others up to 2.1 °, while the reflectivity of the Ir is higher for angles above 0.4 ° at 7 keV. Therefore, the overall effective area at different energies can be improved with the selection of the coating in dependence of the radius of the shell.

The shell radial profiles are shown in Figure 8 (Left): the primary surfaces are drawn in cyan, while the secondary surfaces in blue. The effective area of each shell for Ir and Pt+C coating @1keV, @6keV and @12 keV is shown in 8(Center). In dependence of the incidence angle the more effective coating could be selected, this selection can improve the result in terms of effective area that is calculated in the two cases assuming the same coating for all the shells.

The cumulative effective area of the assembly is reported in figure 8 (Right), starting from the innermost and going to the outermost. The number of shells and their radial position is defined on the basis of the total mirror weight and the effective area reached. The shell does not fill completely the available radial space and there is some margin for the optimization of the shell distribution. In particular there are five radial gaps in correspondence of the spider radial connections needed to reinforce the structure. The effective area reached by the whole mirror assembly as a function of the photon energy is shown in figure 9. The effective area at 1keV is around 2 $m^2$ (with 11 % obscuration from the structure already taken into account) and the mirror weight of the mirror shells (without structure) around 1900 kg.

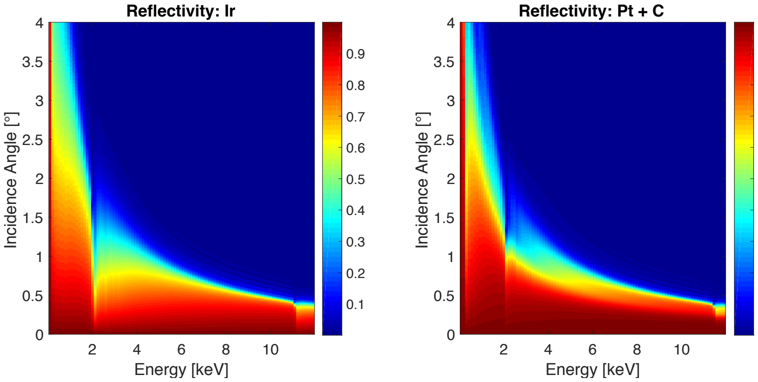

**Figure 7: Reflectivity of the Coating used for effective area evaluation. (A) 40 nm Iridium, $\sigma = 0.5$ nm. (B) 40 nm Platinum with an over coating of Carbon 10 nm, $\sigma = 0.5$ nm.**

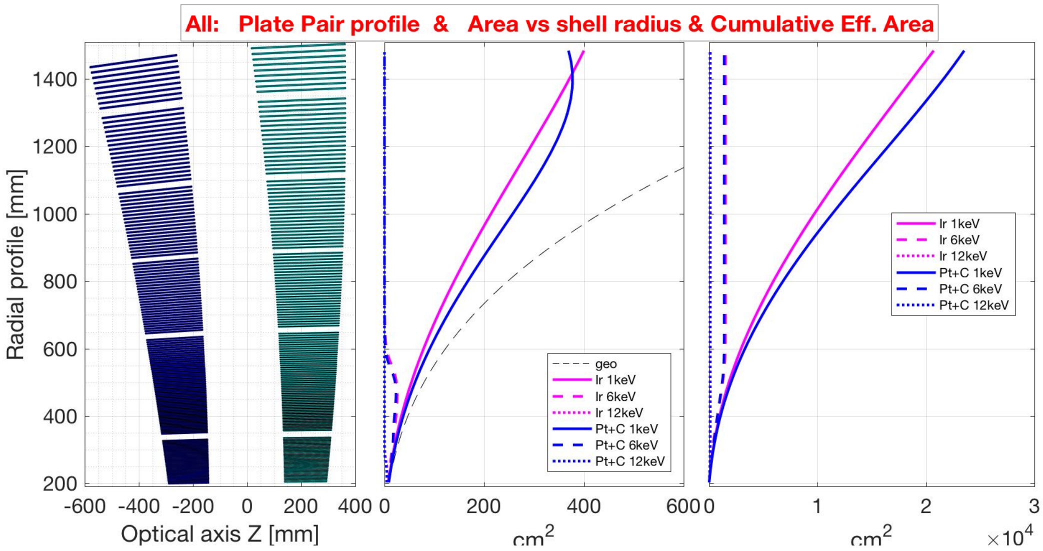

**Figure 8: (Left) Radial profiles of the shell (in cyan the primary surfaces, in blue the secondary surfaces). (Centre) The effective area of each shell for Ir and Pt+C coating @ 1 keV, @ 6 keV and @ 12 keV. (Right) The cumulative effective area of the assembly, starting from the innermost and going to the outermost.**

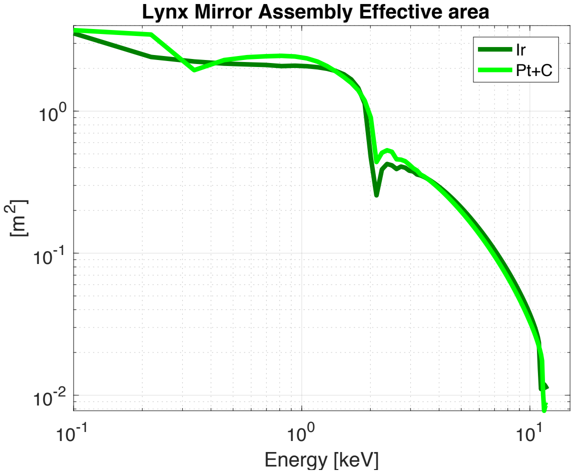

**Figure 9: Lynx Mirror Assembly (LMA) effective area in the 0.1 - 12 keV range. 40 nm Ir coating or 40 nm Pt + 10 nm C are considered.**

The optical performances in the FOV have been evaluated for the LMA with ray-tracing software, taking into account the reflectivity of the surface in dependence of the energy and the incidence angle of the impinging rays. The HEW results are presented in Figure 10 (Left): for each of the energies the best focal plane position is determined and the corresponding HEW reported in the top panel. On the bottom panel the position of the corresponding focal plane is shown. The difference in the focal plane curvature, highlighted in figure 6 for single shells, turn out in a general dependence the focal plane curvature with the energy, as it is directly related to the effective area at a certain energy of the shells. In order to show the improvement of the curved focal plane on the overall performances, in figure 10 (Center) are shown the HEW calculated on a flat focal plane. For off-axis angles greater than 5 arcmin the curved focal plane is indispensable to limit the optical performances degradation. In figure 10 (Right) is shown the general result, assuming only one focal plane, optimized for 1keV photons.

Note that the HEW on axis and for small off-axis values is not zero at low energy. The optimization of the optical performances in the FOV is finalized using the focal plane corresponding to the middle of the FOV (5' arcmin) to define the position the common focal plane. This choice degrades to 0.3'' the optical performances on axis but improve the off-axis behaviour from 1.6'' to 1.3'' at the edge of the FOV. This is particular important to increase the GRASP. The requirement is defined taking into account 1'' HEW limit and 10 arcmin off-axis angle. The vignetting function is determined at different energies with ray-tracing software considering the ray passages at the different interfaces. The results are shown in figure 11 (Left panel) and are calculated up to 12 arcmin. The overall HEW of the LMA, in the assumption of a curved focal plane, is shown on the bottom of figure 11A. The corresponding GRASP is calculated taking into account variable limits in the HEW (between 2'' and 1'' HEW) and variable size of the FOV (between 10 and 12 arcmin). The results are shown in figure 11 (Right panel) together with the required value of 600 $m^2$ * $acrmin^2$. If determined within a FOV of 10 arc minutes and considering values of HEW lower than 1 arc second, the total grasp is slightly below the requirements. The grasp requirement is reached increasing the maximum value for the HEW to 1.2 arcsec.

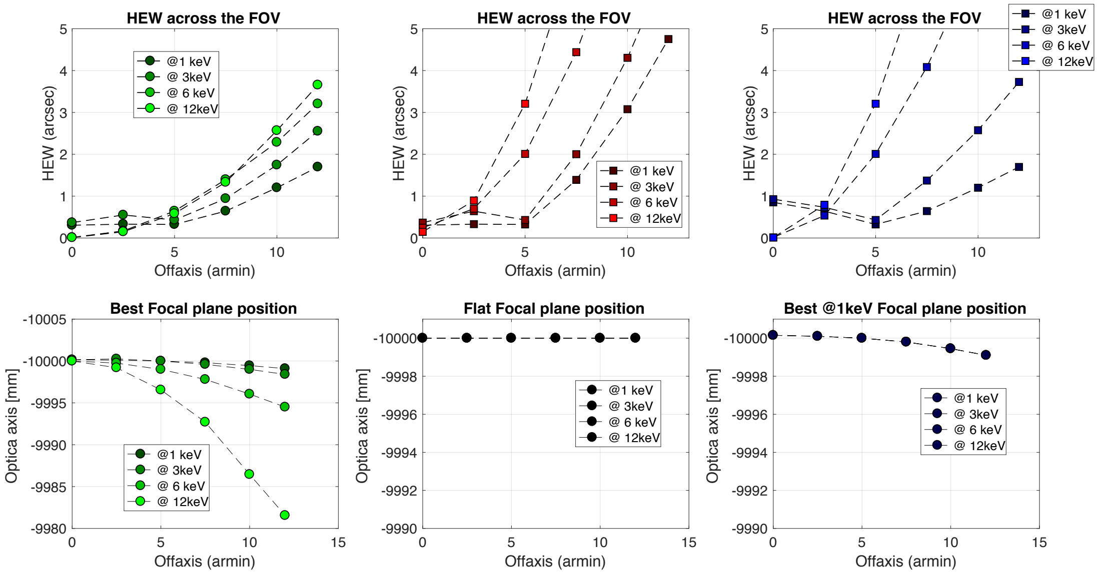

**Figure 10: Ray-tracing results. The HEW (top) and correspondent focal plane positions (bottom): (Left) at best focus positions (Center) on flat focal plane and (Right) on a curved focal plane (best focus positions as derived from 1 keV results). Values are given for each of the off-axis positions (0 , 5 , 10 and 12 arcmin) and at different energies (@1 keV, @ 6 keV and @ 12 keV)**

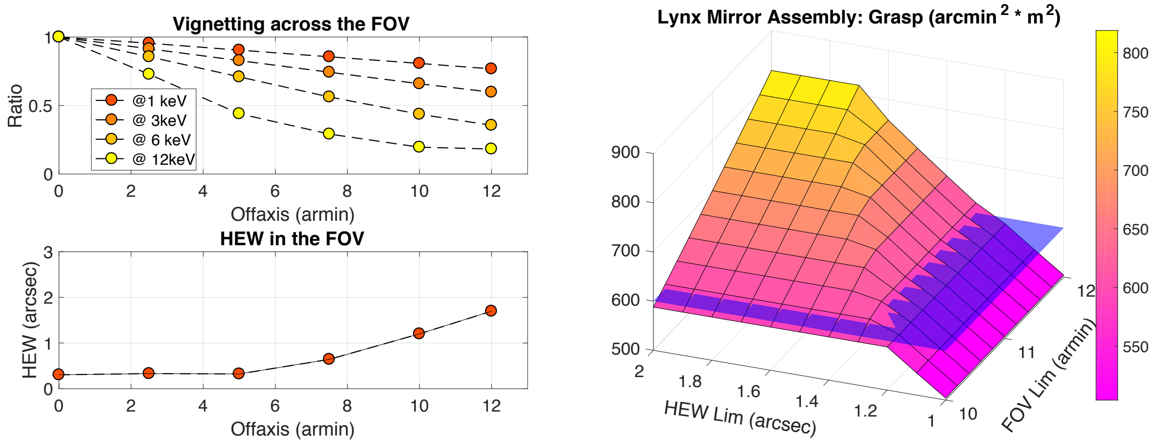

**Figure 11: (Left) The vignetting for off-axis directions up to 12 arcmin @1 keV, @3 keV, @6 keV and @12 keV. On the bottom panel the HEW @1 keV for the same off-axis directions. (Right) The GRASP in function of the FOV considered in the calculation and of the limiting HEW.**

## 4. ERROR BUDGET

The top-level error budget for the mirror assembly realization is reported in table 8. The optical design foresees 0.3 arcsec on-axis HEW @1 keV on a defined focal plane position. Taking into account the contribution of the diffraction of the different shell weighted for their effective area, the total HEW is 0.31 arcsec.

The sensitivity analysis, reported in paragraph 2, returns contributions between 0.03''-0.55'' (for 1° C DeltaT) in dependence of the thermal load distribution. This gives confidence that, with a dedicated thermal control, the thermo-mechanical contribution can be reasonably limited to 0.2 arcsec. As well, the effect of the gravity release has been evaluated trough FEM simulations. The current contribution (0.26 arcsec) was derived with a preliminary design of the SW structure. It could be decreased working on materials, increasing the CFRP Young Modulus to raise the SW stiffness, and on the optimization of mechanical design, refining the design of spoke wheel structure and of its connection to the MS.

The reduction of the thermo-mechanical contribution will increase the margin for the shell manufacturing, which is now set at 0.24 arcsec. This error is distributed between different terms. Simulations return the coating contribution. Assuming a value of tensile stress (350 Mpa, for an Ir coating 35 nm thick), the error contribution ranges between 0.24 arcsec and 0.45 arcsec HEW. Given that this stress value is very conservative with respect to the reality, its reduction is feasible leading to impact of the order of 0.1arcsec HEW. The symmetry of the geometry will also help when the not uniformity of the coating is considered. This is a major advantage with respect to segmented optics, where these deformations need to be avoided or compensated to prevent angular resolution degradations. For segments the same coating would contribute up to a few arcsecs degradation, depending on the radius and the thickness of the mirror segment.

The accuracy of the metrology during the manufacturing process and during the tests limits the performances of the final optic. The error contribution is set to 0.05 arcsec. In principle, reference mirrors and lens can be realized down to 5 nm rms accuracy. Moreover, interferometry set-up, a proper choice of the ground equipment materials and a good thermal control of the environment (0.2 °C), can guarantee a repeatability of the same order.

The handling and the manufacturing the shells are realized with dedicated supporting systems. The analyses showed that the SSS acts differently on the low and high spatial frequencies error. For instance, if we consider the MS deformations induced by MS supports before the connection to SSS, we see that the nominal supporting forces deform the shell with high spatial frequency errors, which are relaxed by the flexures. On the contrary, the errors in the supporting forces generate low frequency errors, which are kept by the system. As long as they will be corrected during the figuring of the shell and no significant spring back is expected after the shell integration into the SW, the contribution of the supporting system can be very low. Preliminary analysis on the SSS returns a 0.05 arcsec contribution.

**Table 8 – Error budget**

| | | | |
|---|---|---|---|
| Optical configuration | 0,31 | | |
| | | 0,3 | :: Design |
| | | 0,09 | :: Diffraction |
| On-orbit loads | 0,33 | | |
| | | 0,2 | :: Thermal |
| | | 0,26 | :: Gravity release |
| Shell manufacturing | 0,24 | | |
| | | 0,05 | :: Metrology |
| | | 0,15 | :: Front mirror figure error |
| | | 0,15 | :: Rear mirror figure error |
| | | 0,05 | :: Shell Supporting System |
| | | 0,1 | :: Coating |
| Integration | 0,18 | | |
| | | 0,15 | :: Alignment error |
| | | 0,1 | :: Bonding |
| Final HEW | 0,55 | | |

The error term related to the optical surface error is set to 0.15 arcsec for both the front and the rear surfaces. Main terms contributing to this error are the longitudinal profile, the azimuthal and the micro-roughness errors. Numerical simulations showed that limiting to around 10 nm rms the profiles error the expected contribution is below 0.1 arcsec HEW (6). Given that azimuthal error impact scale down with the focal length, a 200 nm PtV azimuthal error would contribute 0,05’’ in HEW. Micro roughness values around 0.2 - 0.3 nm (within the standard polishing capabilities) would return negligible contribution in terms of HEW.

The error term related to integration (0.18 arcsec) is split in two main contributions. The alignment term is dominated by the tilt between the optical axis of the front and the rear surfaces. While the rotation around the optical axis has no effects, the contribution of displacement errors can be kept lower than 0.04 arcsec if an accuracy of few microns is reached. Given that only one side of the semi-shell has to be bonded to the spoke wheel, the transfer will be relatively easy, with reduced distortion possibilities. There are several space-qualified epoxies on the market, which can guarantee very low shrinkage. As the number of the shell to be integrated is limited, there are not extremely tight temporal constrains to be taken into account. As a consequence, there are no limitations in the epoxy selection based on the curing time and the set-up of a reliable and smooth bonding process is possible.

## 5. FABRICATION PROCESS OVERVIEW

The manufacturing of the shells is based on the direct polishing according to the steps reported in the following paragraphs.

### 4.1 Shell procurement and initial treatments.

The process starts from the procurement of the shell raw material. Raw fused silica tubes are currently available on the market at affordable costs. The Heraeus Quarzglas GmbH & Co KG normally produces tubes in fused silica with diameters up to 900 mm and wall thicknesses between 0.5 – 13 mm. In the past years, we have already purchased several raw quartz tubes from Heraeus Quarzglas GmbH & Co KG. Starting from a cylindrical shape, they were grinded to a double-cone configuration, with a two-steps grinding procedure. The external and internal surfaces of the glass tubes are both machined by means of a row grinding process. Higher diameters can be achieved with the hot slumping technique: this is feasible and demonstrated by Heraeus with small prototypes. This process, traditionally used to re-size the cylindrical tubes, can be optimized to change from cylindrical configuration to the conical one. This would reduce significantly the amount of material to be removed in raw grinding especially for larger shell. Starting from the conical Fused Silica shell, first grinding operations are performed to obtain the required thickness with tolerances of a few tens of microns with respect to the final conical shape. As stated the process has already been tested for shell with diameters up to 600 mm: a cylindrical tube of fused silica is ready to be grinded to double-conical shape is shown in figure 12 (Left).

Corning Incorporated (USA) may also provide fused silica shells and the realization of very large diameter shell (up to 3 m) is already in the company capabilities. In this case the shells are cut via water-jet from a chunk of fused silica and then grinded. The outemost shell lenghts are of the order of half a meter: they are compatible with this production conpcet.

The process to generate the thin shells may introduce stress in the material. The characterization of the residual stress will be carried out in the next phases of the project, on the basis of the supply chain that will be chosen. In case, a proper annealing procedure may be studied to relax the stresses in the material.

During the manufacturing process, the internal and the external surfaces undergo grinding operations. While the Sub Surface Damage (SSD) is removed on the internal surface during the different polishing phases, but the treatment with a chemical etching could address the problem for both the internal and external surfaces at once. The assessment of this process will be the subject of further studies. As the strength of the glass depends on the surface quality [9], the removal of SSD is particularly important for the mechanical modelling of the system. Higher glass strength simplifies the design of the LMA, increasing the resistance of the shell to launch loads. Moreover, it enables higher polishing force, with positive impact on the polishing speed. As the polishing time for large shell is not negligible, a faster polishing process will be very helpful in the overall manufacturing process of the shells.

### 4.2 Shell Support System (SSS)

The realization of thin shells is possible by taking advantage of the intrinsic stiffness of the monolithic shells and adopting an ad hoc integration concept based on a Shell Supporting Structure (SSS) jig [10] to be used for the handling and to support the shell in all the manufacturing steps (grinding, polishing, X-ray calibrations). The SSS dimensions have to be coherent with the shell diameter and length.

The SSS is designed to follow the shell up to the final integration in the spoke wheel. This handling system interfaces the different figuring equipment, limiting the deformations experienced by the shell. It is based on a metallic thin "comb", glued with a dedicated adhesive, which realizes a radial flexure at the connection between the mirror shell and the external rigid structure.  The goal is to minimize radial forces on the MS. Loads are transmitted tangent to the MS wall, i.e. in the stiffer direction, minimizing MS distortions. A similar system has been already designed and used for thin glass shells manufacturing [11]. The integration into the SSS is a delicate phase. In order to limit to the minimum the deformations induced by the gravity, the shell is sustained with an astatic support. The tolerances for the manufacture of the system (three fixed positions and N additional supporting points on calibrated air bearing) will be studied and analysed taking advantage of the experience made during the integration of different shells. A prototypal double conical shell supported on the astatic support currently available at INAF/OAB is shown in figure 12 (Center), while in figure 12 (Right) is shown the shell after the integration into the SSS.

The current SSS design will be revised in order to be compatible with the tighter requirements of the LMA shells. In the future, two other major changes are foreseen. First, the double glass rings structure will be transformed in a stiffer system probably made of CFRP. Second, the radial flexure will be realized only on one the sides of the shell, near the edge to be fixed to the spoke wheel.

### 4.3 Fine Grinding

The geometry of the semi-shell is almost conical, with specific profiles along the shell meridians. In order to bring the optical surface near to the target, several tens of microns (as a minimum) should be removed from the surface, both along the azimuthal direction (errors in the roundness) and both along the longitudinal directions. The Out-of-Roundness (OOR) and the profiles correction are obtained by means of fine grinding process.

So far, the fine grinding operations were performed at LT Ultra Precision Technology GmbH by means of a high accuracy diamond turning lathe equipped with grinding wheels [6]. The grinding phase on thin shells is shown in figure 13), while a detail of grinding wheel acting on a flat sample is shown in figure 13 (Right). In the current set-up, we stopped the correction of the OOR at around 1.5 microns Peak-To-Valley (PTV) errors. From a general point of view, the impact of this error depends from the phase (in-phase or out-of-phase) of the residuals on the primary and on the secondary surfaces. Therefore, the degradation of the angular resolution of the shell was evaluated trough ray-tracing simulations assuming the acquired metrological data to define the azimuthal profiles. In order to reach the target PTV errors (of the order of few hundreds of nanometres), the same process could be adopted in the future, apart for what concerns the shell orientation. In dependence of the SSS design, it could be necessary changing the set-up to the vertical condition. In general, different optical probes, which guarantee high accuracy and low noise, are available on the market. They can be mounted directly on the lathe, allowing a pretty fast and accurate metrological system. The same scheme could be used from the very first phase of the process when the surface is rough.

### 4.4 Polishing phase.

At the end of the grinding process and before starting the polishing phase, the SSD on the surface have to be removed. Mechanical or chemical approaches could be used. While the chemical etching has not been yet investigated, a pre-polishing phase with the Bonnet tool has been successfully tested. It guarantees an efficient SSD removal. This DC removal does not change the profiles error but brings the micro-roughness below 10 nm RMS on the millimetre scale. At this level the surface become measurable with an interferometry approach. This pre-polishing process can be carried out on a directly on the grinding lathe by means of bonnet (not inflated but filled with rubber), see Figure 14 (Center) [6]. As well, it can be operated directly with a standard Zeeko Machine [11,12]. These machines work on the concept of dwell time.  They combine a rotary stage and 6 axis robotic arm, with a complete control on the relative position of the tool and the surface: a finer correction of the residual azimuthal and longitudinal errors (down to the size of the tool print-trough) could be implemented. As a drawback, the accuracy in the positioning is poor and the stages of the machine cannot be used directly for moving a probe for the metrology.  Therefore a different metrological approach has to be used or, alternatively, an ad-hoc machine realized.

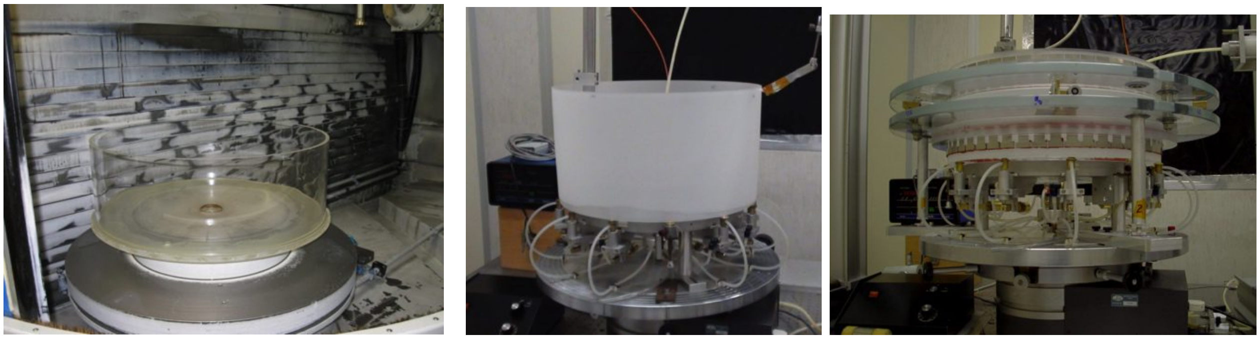

**Figure 12: (Left) A cylindrical tube of fused silica before the grinding to generate a double conical configuration. (Center) The shell after the raw grinding ready to be integrated in to the SSS. (Right) A astatic equipment is used to support the shell during the fixation to the Shell Support System (SSS).**

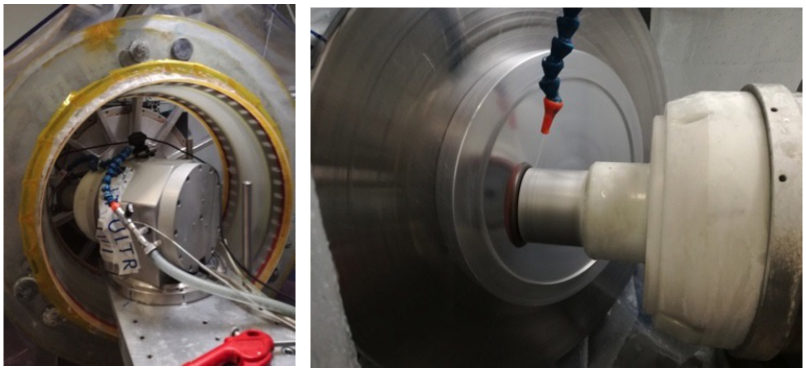

**Figure 13: (Left) The shell on the lathe during the grinding phase. (Right) The detail of the grinding wheel during tests on samples.**

**Figure 14: (Left) The polishing phase with a pitch tool. The shell is mounted on the lathe with the optical axis in horizontal position. A liner carriage drives the oscillations of the pitch tool along the optical axis. $CeO_2$ slurry is distributed. (Center) The lathe is equipped with a bonnet tool. The $CeO_2$ is dispensed trough the nozzle, reproducing the nominal Zeeko set-up. (Right) A new polishing set-up is tested on the shell. A layer of TRizact 3M covers the pitch tool. Demineralized water is used instead of slurry.**

The smoothing of the mid-frequencies is achieved by means of pitch-polishing (Figure 14 left). This phase could be implemented on the same precision lathe making use of a pitch tool device. In order to speed up the process and reducing the polishing time, an additional stage can be used to drive the tool with high frequency: while the shell rotates around the optical axis, the linear stage oscillates parallel to the surface of the shell. The process can be optimized with respect to different parameters as the kind and the grain of the abrasive, the length of the movement, the pitch tool size, its oscillation frequency and the force exerted. The target of this process is to achieve an error of about 1.3 nm RMS on spatial wavelengths between 2 mm and 10 mm and around 5-10 nm rms on longer scales. New kind of abrasives, like TRizact 3M have been proven an effective solution: the usage of demineralized water instead of slurry is a great functional advantage in this kind of process and it reduces the cleaning time [6,13] (Right panel of Figure 14). Furthermore, it can be used down to the very last steps of polishing as it easily guarantees micro-roughness below 1 nm rms on the millimetre scales. With the correct settings in terms of pitch/abrasive/slurry parameters, the same kind of oscillating pitch tool can be used for the final super-polishing of the shell, aiming at reaching a micro-roughness level below 0.5 nm RMS.

### 4.5 Ion beam figuring.

At the end of the polishing activities, the accuracy on the longitudinal profiles is expected to be of the order of a few hundreds nanometres PTV. This final error can be the sum of different factors, as the errors remained after the initial calibration of the stages and or the thermal effects. Moreover, due the floppiness of the shell, the standard direct polishing approach (e.g. not based on dwell time) could introduce errors in the surface.

As long as the surface micro-roughness is lower than 0.5 nm RMS, the longitudinal low frequency profile errors are theoretically correctable with an ion beam figuring process, without degrading the micro-roughness [14]. We intend to test this high accuracy figuring process on the shell by using the large ion beam facility developed in the past years at INAF/OAB [15,16]. This facility, originally designed for large aspheric optics with diameters up to 1.3 m, is being up-graded, allowing the ion figuring of grazing-incidence shells. In order to apply the ion beam correction, the shell will be placed inside the chamber with the optical axis aligned as the gravity and a rotary table will manage the shell rotation during the ion figuring.

From a general point of view, the removal rate decreases during the different steps. The lower is the initial error, the faster will be the manufacturing step. Nevertheless, the transition between the process phases could be optimized taking into account their convergence rate in the different steps.

### 4.6 Coating

The coating is applied on the shell at the end of the polishing phase, while supported on the SSS. The vacuum chamber for the deposition should be large enough to host the SSS, no other constrains apply in the set-up. The combination of ion beam figuring and the coating in the same vacuum chamber could be considered in terms for cost reduction, in particular for large diameters shell. Further evaluations, with respect to the overall production schedule, should be taken into account for a complete assessment of the benefits.

As long as the thickness and the stress of the deposit are kept constant along the shell surface, the symmetry of the close shell condition mitigates the deformations induced by the coating. A coarse hand assessment evaluation of the expected edge effects may be made by means of the elastic theory of long pipes. Considering a deposit 35 nm thick tensioned with 350 MPa, the expected distortions are quite low (e.g. less than 0.1 micron radial displacement and less than 1 arcsec deformations) and the effects damp exponentially along the Mirror Shell axis. In this condition, the expected impact on the HEW is very low. As the value of stress is quite conservative and the results can be scaled down linearly. The symmetry of the geometry will also help when the not uniformity of the coating is considered. This is a major advantage with respect to segmented optics, where these deformations need to be avoided or compensated to prevent angular resolution degradations. For segments the same coating would contribute up to a few arcsec degradation, depending on the radius and the thickness of the mirror segment. The firsts test on the coating will be carried out in the next phases.

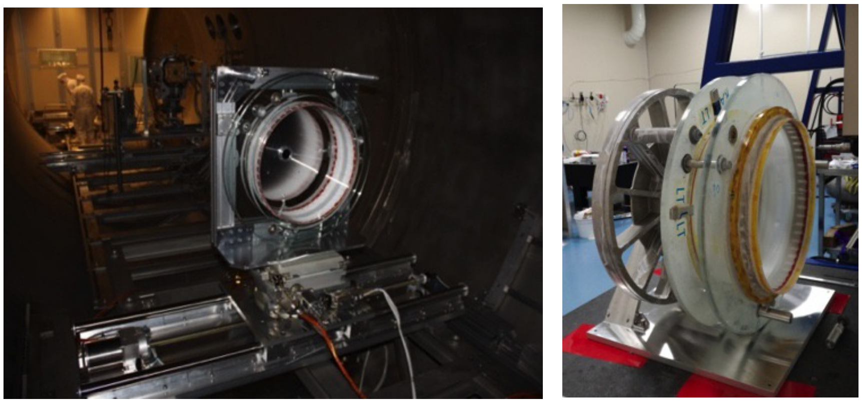

**Figure 15: (Left) The jig used to support the SSS with the shell#7 during the measurements @Panter in 2011. (Right) The Invar Spoke Wheel (ISW), added to the SSS during the manufacturing of the Shell#4, is interfaced to the new jig for calibration.**

### 4.7 Integration into the spoke wheel.

Once ready, the shell has to be transferred into the Spoke Wheel. In case, intermediate x-ray calibrations can be exploited at the end of the different phases of manufacturing, while the shell is still supported on the SSS. In particular, a final x-ray characterization could be envisaged before the final integration. Out of focus measurements could confirm the best relative rotation (around the optical axis) of the two semi-shells, which can be derived on the basis of the metrological data. The defects, if any, could be concentrated in the same azimuthal area so that they can be masked with a minimum loss of effective area. On the contrary, it would be possible to optimize the throughput of the two semi-shells, compensating for the residual errors on the front with the ones on rear surface. The semi-shells are bonded on the SW while they are still integrated in the SSS. As described in Section 2, the integration is foreseen in vertical configuration and in a 'constant mass' condition. Therefore, a distribution of dummy masses, simulating the presence of the missing shells, is envisaged. Furthermore, a dedicated off-loading system, to reduce effects at the gravity release, is foreseen.

From the operational point of view, front semi-shells (first reflection) are bonded on the smaller diameter, while the rear semi-shells (second reflection) on the larger. While the rear semi-shell can be nested from the bottom without particular mechanical constrains, the front semi-shells are nested from the top. The current optical design is compatible with this scheme, as it respects the correct diameter sizing of consecutive semi-shell. In principle no temporary bonding to additional structure is requested and the shell is transferred to the spoke wheel interfaces on the same side where the SSS is supporting the semi-shell. This helps avoiding undesired deformations.

### 4.8 X-ray calibrations.

Thanks to the mounting in the SSS, the x-ray calibrations of the shells can be performed, if needed, at different manufacturing stages. This is a very useful possibility, in particular during the first part of the development phase. As long as first x-ray measurements may be pursued after the polishing phase, they can be used to validate the metrological set-up and the mounting concept itself. A crosscheck can be done between the measured results and the expected HEW derived from the metrological data and mechanical simulations. A second calibration run can be foreseen once the final ion-beam figuring process is done, when all the figuring activities on the shell are completed, with the goal to reach a sub-arc second angular resolution. Finally, the final x-ray calibration will assess the optical performances after the integration into the mirror structure of the entire set of mirror shells.

A calibration of a thin old prototypal shell in an intermediate stage of the polishing process has been already performed in 2011. The calibration was realized in Panter/MPE and the set-up is shown in figure 15 (Left) [11]. The interface between the SSS and the facility was realized with a simple frame of aluminium, holding the SSS. In that configuration, the poor stiffness of the system could arise problems, as the distortions in the SSS introduce deformation in the shell. The problem was solved with the up-grade of the SSS (with an additional invar wheel interface) and the design up-grade of the holding system. The new set-up is shown in figure 15 (Right), during the metrology in INAF/OAB.

## 6. RECENT TESTS ON PROTOTYPAL SHELLS

The realization of thin fused silica monolithic shells started as part of the feasibility study of the WFTX mission concept [11]. For that mission concept, three X-ray mirror modules based on around 60 shells were needed to reach a total effective area of 1 m$^2$. In each module, the shell diameter was ranging between 300 mm to 960 mm, with a focal length of 5 meters. To limit the weight of the mirrors, the shell thickness were in the 2-3 mm interval. The main difference with respect to the current design is the fact these shells were almost double conical. In this case, the front and rear optical surfaces were joined at the intersection plane.

The general feasibility of the direct polishing approach on thin glass shells was demonstrated in 2012 (TRL3), using a process pretty similar to one described above. A prototypal shell was manufactured (Shell#7), with a polynomial optical design and with a small aspect ratio. Starting from a raw grinded fused silica shell produced by HERAEUS (Germany), a double-cone shell was precisely grinded by LT-Ultra (Germany). A deterministic polishing and figuring process was then applied by means of IRP600 Zeeko machine based on bonnet polishing in order to impose the polynomial Wolter-like profile adopted for WFXT. Then, a pitch super polishing process was implemented using a dedicate pitch tool mounted on the IRP600 arm. An intermediate x-ray calibration was carried out at Panter/MPE (with TRoPIC detector) to crosscheck the performances with the available metrological data. In order to follow as much as possible the focal plane curvature, the images have been acquired at the best focus of each angular position. X-ray data (0.93 keV) have been collected on axis, at 10’, at 20’ and at 30’ off-axis angles. As expected, the measured HEW was quite flat across the FOV. The values recorded vary from 17.8” on-axis up to 23.7” at 30 arc minutes off-axis [11]. The ray-tracing simulations based on metrological data can explain the X-ray calibration results with the following error terms. The low frequency longitudinal profile errors contribute 6” to the final angular resolution on the on-axis data. The HEW increases to 8”, adding the OOR (Out-Of-Roundness) contribution. It reaches 12’’ considering the tilt between the optical axes.

The measured HEW is reached considering the longitudinal profile mid-frequencies contribution. The surface micro-roughness, measured around 1nm RMS, brings to a negligible contribution at low energy. The results of this intermediate x-ray measurement showed that the major drivers for improving the shell optical quality were the correct reciprocal alignment of the optical axis of the two reflecting surfaces and the reduction of the mid-frequencies errors. Unfortunately, the shell was damaged during the post-calibration measurement activities and the programmed final polishing on this shell could not be carried out.

The development of a new shell (Shell#4) started in 2013 on the basis of a standard Wolter-I design. In order to overcome the problems faced with Shell#7 and to reach sub arc-sec performances, the production flow of the shell has been partially modified and a final step with IBF was envisaged, as it could account the requested figuring accuracy. The polishing of the shell wasn’t completed mainly due to lack of funds. The work on this shell has been restarted in 2017 thanks to a dedicated founding program of the Italian Space Agency (ASI). The summary of the activities and the final status of the shell are reported in [6]. The original SSS was composed of two rings made of Borofloat glass, hosting three couples of metallic connections. The stiffness of this structure was poor and deformations were induced on the mirror shells during the different fixation phases. An additional interface to the SSS was introduced in order to overcome this problem. This Invar Spoke Wheel (ISW) was designed to follow the manufacturing process of the shell (grinding, polishing, X-ray calibrations) up to the final integration in the spider. The increased stiffness of the system prevents the deformations on the shell, for example, when it is transferred from the lathe to the jig for x-ray calibration. The activities on the shell restarted from the grinding phase. As the OOR to be corrected was not that high, it has been decided to operate starting from the D20 grinding wheel, which guarantees an acceptable removal rate without degrading too much the micro-roughness. At the end of the grinding phase, as the metrology on the lathe is relatively simple, a bonnet polishing has been applied directly on the lathe in order to reduce the SSD. The lathe configuration was modified and a dedicated mixing device at controlled temperature was purchased for the slurry distribution. A mechanical interface has been prepared for the fixation of the Bonnet tools on the spindle. Unfortunately, the shell was broken due to a wrong carriage movement, during the metrological phase of the last run of bonnet polishing. The breakage passes through the shell height completely. An UV curing adhesive was used to fix the shell and the initial plans were changed. Due to the shell fracture, it was not possible to operate on all the shell, as the pitch tool could be damaged passing above the fracture. A limited test of the next polishing phases was carried out on an azimuthal portion of the parabolic section. Then the shell was dismounted from the lathe at the beginning of august 2017.

At the beginning of 2018, the test activities restarted by means of the available equipment in INAF/OAB laboratories, with the aim of complete the figuring of an azimuthal segment of the shell#4. The Zeeko IRP1200 [17] was used both for Bonnet polishing and both for the pitch polishing. A new set-up, based on the interferometric approach, was prepared for the metrology of the shell.

In the past, IRP600 Zeeko machine was used to polishing the Shell#7. Even if the geometry of the new shell#4 is pretty similar, the mechanical constrains on this new IRP1200 Zeeko machine are different. Moreover, as the area to be polished was limited to an azimuthal segment, the set-up and the procedure had to be revised.

In general, the polishing of the internal surface shell is operated combining the rotation of the rotary table and movement of the arm, in vertical and radial direction to follow the conical angle of the surface. Moreover, the bonnet tool is driven on the surface with a precession angle. Given that the machine works on the dwell time, the tool path is generated from the Zeeko software, based on the geometry of the surface and of the error to be removed. Moreover, the tool patch follows the real relative alignment between the surface and the bonnet, in such a way that the applied offset is constant on the surface. The greater is the offset is applied toward the surface, the higher will be the removal rate. Given that the shell is thin and changes shape when pressed, the maximum allowable offset has been derived in terms of maximum radial allowable deformation. This corresponds to a maximum load, which was derived by mechanical simulations. Taking into account that some margin was taken due to the lack of experimental data on the glass strength, the velocity of the process could be higher in the future, when the data relevant to the material characterization will be available.

Due to the presence of the breakage on the shell surface, only an azimuthal section of the shell has to be figured. This kind of geometry is not considered in the options available in the Zeeko software. A reverse engineer approach was used in order derive, from the standard case of a complete revolution surface, the basic inputs for the process (like precession angle, commanded relative positions for the robotic arm path), which were used to generate a custom G-code for the operations. Probing the surface in different positions, the position and the alignment of the surface segment have been reconstructed and accounted for a constant offset application. The tool path was set to a raster scan, moving along rows, and starting from the top. The rotary table movement drove the scan of each row, with inversion of the motion at the edge of the azimuthal section. The passage between rows was handled in the same area. In the pre-polishing phase a constant removal was requested, so that the relative velocity between the surface and the tool was the same in all the area. The tool path for the pitch polishing was generated in a different way. A number of azimuthal positions have been randomly generated. In correspondence of each of them, the pitch tool was driven up and down along the vertical axis following the conical angle with radial corrections. The number of strokes, their amplitude and the position of the centre of oscillation could be defined. The azimuthal scan are repeated back-and-forth for a defined number of times. Given the randomization on the angles, each scan is independent from the previous one.

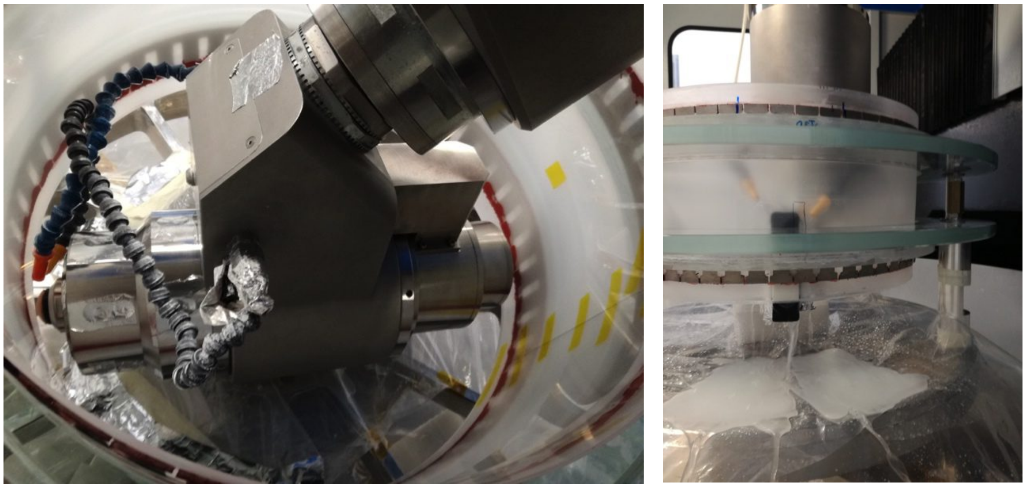

**Figure 16: (Left) The Zeeko IRP1200 equipped with the Bonnet R20 is used @INAF/OAB to polish an azimuthal segment of the shell#4. Given the relative size of the shell and of the robotic arm, the accommodation of the shell was not simple. The precession angle is reduced to 10° and set in horizontal direction. In this way the shell fits with few millimetres margin. The breakage occurred on the lathe is visible on the right. (Right) The pitch tool equipped with TRizact 3M$^{TM}$ is fixed on the robotic arm of the Zeeko machine and the vertical carriage movement has been used to move the tool up and down.**

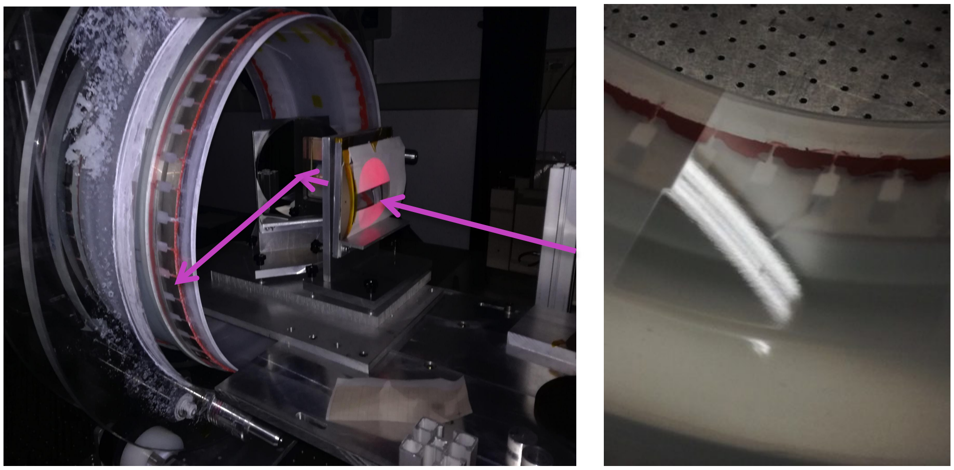

**Figure 17: (Left) The metrological set-up used at INAF/OAB to control the smoothing process during the polishing. (Right) The azimuthal section of the shell under machining.**

Figure 16 (Left) shows that the robotic arm of IRP1200 fits the shell#4 with a margin of a few millimetres. Nevertheless, the working condition is very safe, as the approaching and the departure phase are based on the same G-code, which drives the polishing. The movements of the robotic arm are given in terms of positions and orientations in the machine system reference. Once checked a first time, the operations can be realized automatically. This is a very safe condition with respect to the procedure adopted on the lathe, where the movements at the beginning and at the end of the machining had to be commanded in manual way. The breakage of the shell#4 occurred during one of these phases.

In the past activities with IRP600 Zeeko and in bonnet polishing phase experienced on the lathe, the R40 Bonnet tool was used in the figuring. It guarantees a good removal rate with a footprint of around 1 Centimetres Square. Given the different sizing of the robotic arm of the IRP1200 Zeeko machine, the usage of the R40 bonnet became impossible. A smaller bonnet (R20) was the only possibility to fit the size of shell. The removal rate of the R20 is a factor four lower with respect to R40, with a considerable increase of the polishing time. Due to mechanical interference, the standard precession angle (20° with respect to the vertical) was not implementable and an alternative configuration was used. The precession angle was reduced to 10° and set in horizontal with respect to the surface. In general, the lower is the precession angle, the lower is the expected micro-roughness. As a drawback, the removal rate is lower. With a further reduction of a factor two due to the lower precession angle, the process was a factor eight slower.

The smoothing procedure has been used with the same process tested on the lathe [6]. A pitch tool with a layer of Trizact 3M [13] has been fixed with bi-adhesive. The linear stage, used on the lathe to allow the high frequency oscillations of the pitch tool, is too heavy to be mounted on the Zeeko robotic arm. So, the pitch tool movement was driven directly by the Zeeko carriages (Figure16 right panel). As a consequence, taking a minimum margin on the maximum carriage velocity, the resulting oscillation frequency is a factor 10 lower. Therefore, the results achieved in this configuration should be scaled for temporal assessment considerations. The length of the stroke has been increased to 5 cm and the length of abrasive area reduced to 80 mm.

Given that the weight of the overall assembly (Shell + SSS + ISW) was about 80 kg, it has been decided to keep the ISW fixed on the Zeeko rotary table and move only the Shell in the SSS for the metrology. The connections between the ISW and the SSS were changed to spacers allowing a kinematic mount. The micro-roughness has been evaluated with MFT 10x on the scale of 1 mm. The longitudinal profiles have been measured with Zygo interferometer. The set-up is shown in figure 17 (Left). The collimated beam passes trough a cylindrical lens and reflected with a flat mirror at 45° before hitting the surface of the shell. This kind of metrology is feasible, in dependence of the amplitude and the amount of mid-frequencies present on the surface. In particular, during the first part of the smoothing, it returns only qualitative assessments. A new system, which combines the Out-Of-Roundness profilometer measurements with an optical probe and longitudinal scan acquired with the interferometer, is under study and could be build starting from the available equipment. In figure 17 (Right) the azimuthal segment under figuring is shown

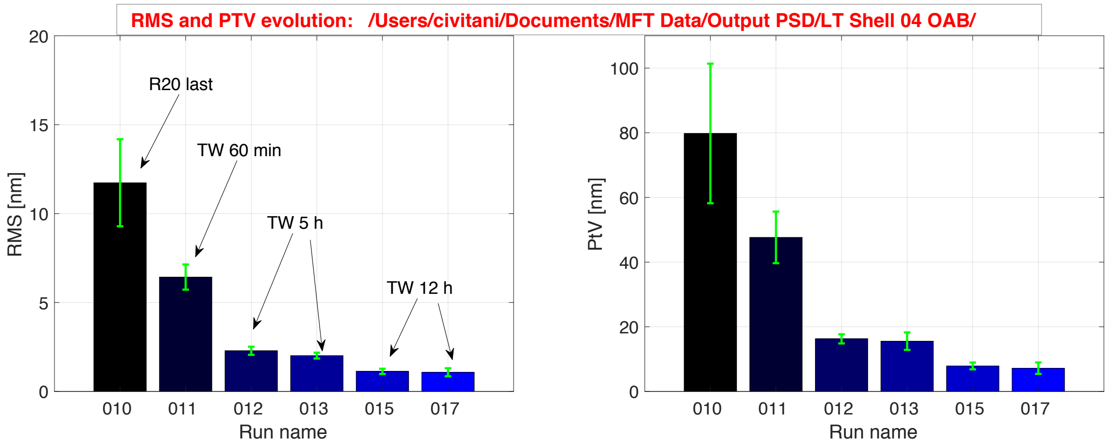

**Figure 18: MFT 10x measurements results in terms of rms and PtV during the TRizact polishing phase. First data is relevant to the status of the segments after the last Bonnet polishing run. After around 20 hours the process converge to around 1 nm rms.**

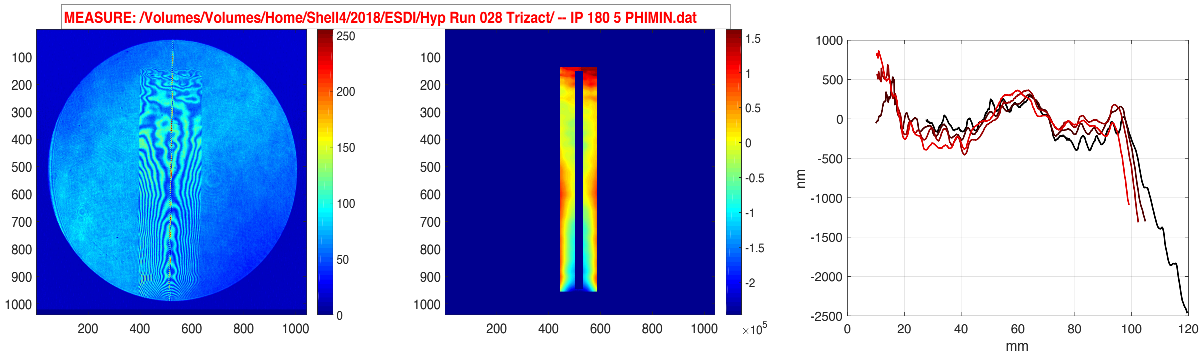

**Figure 19: (Left) The fringes pattern during the measurement with the interferometer. (Center) The reconstructed error map. (Right) The evolution of one profile extracted from the maps corresponding to the last four polishing runs.**

The rms and the PtV of the micro-roughness maps acquired on 1 mm scale are reported in Figure 18. The values correspondent to the last run of Bonnet polishing were around 12 nm rms. This is an improvement with respect to the pre-polishing operated on the lathe (when the process converged to around 25 nm rms due to the slurry density deposition) and it is mainly due to the reduction of the waviness on the mid-frequencies scale. 47 hours were spent in total for this pre-polishing phase. The polishing with the Trizact converged quite rapidly in terms of micro-roughness. In the figure the rms is halved in one hour and then arrives to around 2 nm in 6 hours total. The process converges to around 1 nm rms in 17 hours.

In the current configuration, the time scale is even longer with respect to the mid-frequencies smoothing. The fringes pattern during the measurement with the interferometer of one of the last polishing run is reported in figure 19 (Left). The mid-frequencies features are localized in the edges of the considered segment. The reconstructed error map is shown in figure19 (Center), colour map is in nanometres. The evolution of one profile extracted from the maps corresponding to the last four polishing runs is shown in Figure 19 (Right). The smoothing effect is visible but the process is not completed. As each of these runs lasts 24 hours, the convergence of the process is at the moment still quite slow. The low frequency error is almost stable for the most part of the area. Given that the micro-roughness level is already sufficiently low, in the next weeks a first trial of ion beam figuring will be tried with the aim of verifying that the shell mounting scheme, the set-up and first evaluations on the problems which could arise from the generated heat and from the back-sputtering. Then, the figuring of the segment will be completed, with respect to the mid-frequencies smoothing and to the final correction of low frequency errors with the ion beam.

## 7. PLANS FOR THE FUTURE

The roadmap for the technology maturation is defined taking into account the TRL milestones requested for the Lynx Mirror Assembly Trade (LMAT). The definitions are reported in table 9. They specify the angular resolution and the fidelity with respect to the final hardware of the breadboards.

TRL3 is achieved with the complete test of the figuring process on a section of shell. In particular, this includes the IBF, as this step of the process has never been tested on a close shell. The demonstration will be realized on a sector of the broken shell#4.

The manufacturing of a complete semi-shell is expected at TRL4: a single-reflection shell will be fully figured, polished, super-polished and corrected by means of ion-figuring. Moreover, the transfer to a breadboard ISW will be verified, proving that the shell optical quality is not degraded. If the feasibility of transfer is demonstrated, the main maturation step of full shell technology is achieved.

The remaining part of the roadmap is expected to run smoothly, being just a repetition of the concept for larger shells. TRL5 is achieved with a composition of larger semi-shells. In this phase the co-alignment between semi-shells will be tested. An alignment concept similar to the one of AXAF could be implemented. In dependence of the available founding, the test could be realized on larger diameter shells (the maximum diameter settable at Marshall/XCRF is 1.4 m). As new equipment would be necessary for the manufacturing of the shells, as an alternative the breadboard could be realized maintaining almost the current sizing, but the practicability of the large mirror shell production should be proven. Furthermore, the feasibility of their supporting system should be verified trough metrological approach.

The supply chain for the provision of the raw shells, compatible with diameter up to 3 m, will be fixed in the next months and the new semi-shell will be purchased to start the breadboard manufacturing activity. In parallel, the characterization of the materials will be performed in order to get proper inputs for a reliable structural analysis. The internal stress of the raw mirror shell is necessary for a trustworthily simulation of the spring back after the integration into the mirror structure. The strength of the $SiO_2$ should be characterized for an assessment of the environmental loads during manufacturing and at launch. In particular these tests should follow the individuation of a reliable chemical etching process to reduce the SSD on both the sides of the shell. The resistance of the glass is expected to increase, with benefits for the structural analysis and the manufacturing process optimization.

**Table 9 – *Milestones* for achieving TRLs for the Lynx Mirror Assembly**

| | **TRL3** | **TRL4** | **TRL5** |
|---|---|---|---|
| Time | 2018 | 2020 | 2024 |
| HEW | 3’’ | 1.5’’ | 0.75’’ |
| Laboratory demonstration conditions | To be achieved on azimuthal segment of the shell under manufacturing | X-ray test of a single coated, using a breadboard lab mount (600 mm diameter) | X-ray test of co-aligned, coated, realistically mounted mirror pairs (p-s) of 2 diameters. |
| Additional requests | | Alignment of a single primary shell, aligned to optical axis as defined by the mount. | Fabricate outermost full shell and demonstrate support structure capability and performance with metrology<br>or<br>X-ray test largest diameter (~1.4 m) that XRCF can accommodate. |

## 8. CONCLUSIONS

Lynx is an X-ray mission concept based on mirror assembly with superb imaging capabilities, large effective area and extended FOV. The mirror assembly realization is a very challenging technological task. Several approaches are being considered to meet the required mirror accuracy. The ‘full shell’ concept is based on monolithic fused silica shells. Given the mass constrains, their thickness should be lower than 4 mm for mirror shells up to 3 m diameter.

In this paper we presented the opto-mechanical design of the mirror assembly, which fulfils the requirements. The design is based on a central spoke wheel, holding the semi-shells of front and rear surfaces on opposite sides. The simplicity of the design is boost by the adoption of monolithic shells, so that the number of items to be realized is limited to few hundreds. The top-level error budget has been discussed in relation to the allocations settable by the preliminary optical and mechanical evaluations. The proposed manufacturing process, based on direct polishing and ion beam figuring, is compliant with the requested tolerances. A support structure is being finalized to sustain the semi-shells during the figuring and polishing operations and to manage the handling until their integration into the telescope structure. The design will based on the experience made with the SSS, used so far for double conical thin shells.

The preliminary results, achieved so far on a breadboard shell have been discussed. Due to a breakage on one section of the shell, the polishing configuration is not straightforward as the azimuthal symmetry guarantees for full shells. Nevertheless, in order to have a clear process overview, the figuring of a section started from an area of the hyperbolic section, which experienced only the grinding phase. We proven the Bonnet pre-polishing step with the Zeeko IRP1200 machine, available at INAF/OAB, realizing an ad-hoc tool path for an azimuthal raster scan. The mid-frequency smoothing, implemented directly on the machine robotic arm, is in progress but runs quite slowly due to the equipment constrains. The up-grade of the IBF facility has been completed, with the introduction of a rotary table and of a new ion gun compatible with the size of the shell. The azimuthal sector will be figured in the near future, probing the concept of the ion beam figuring on a close shell for the first time.

With respect to the future plans, the technological maturation roadmap is delineated in terms of milestones, defined in accordance with NASA TRL definitions. The main technological achievement is expected in 2 years, with the realization of a complete thin semi-shell and its transfer in a breadboard spoke wheel.

## ACKNOWLEDGMENTS

We thank the Italian Space Agency -ASI for its support with a contract focused on glass shell development for X-ray optics (Accordo ASI INAF 2015-041R.0 - Glass Technology for the next generation X-ray optics). We would also like to thank NASA Headquarters for their support to the study of the Lynx mission.

## REFERENCES

(1) O'Dell, S.L., Allured, R., Ames, A.O., Biskach, M.P., Broadway, D.M., Bruni, R.J., Burrows, D.N., Cao, J., Chalifoux, B.D., Chan, K.-W., Chung, Y.-W., Cotroneo, V., Elsner, R.F., Gaskin, J.A., Gubarev, M.V., Heilmann, R.K., Hertz, E., Jackson, T.N., Kilaru, K., Kolodziejczak, J.J., McClelland, R.S., Ramsey, B.D., Reid, P.B., Riveros, R.E., Roche, J.M., Romaine, S.E., Saha, T.T., Schattenburg, M.L., Schwartz, D.A., Schwartz, E.D., Solly, P.M., Trolier-McKinstry, S., Ulmer, M.P., Vikhlinin, A., Wallace, M.L., Wang, X., Windt, D., Yao, Y., Ye, S., Zhang, W.W., Zuo, H., "Toward large-area sub-arcsecond x-ray telescopes II," Proc. SPIE9965, 996507 (2016)

(2) Jessica A. Gaskin, Ryan Allured, Simon R. Bandler, Stefano Basso, Marshall W. Bautz, Michael F. Baysinger, Michael P. Biskach, Tyrone M. Boswell, Peter D. Capizzo, Kai-Wing Chan, Marta M. Civitani, Lester M. Cohen, Vincenzo Cotroneo, Jacqueline M. Davis, Casey T. DeRoo, Michael J. DiPirro, Alexandra Dominguez, Leo L. Fabisinski, Abraham D. Falcone, Enectali Figueroa-Feliciano, Jay C. Garcia, Karen E. Gelmis, Ralf K. Heilmann, Randall C. Hopkins, Thomas Jackson, Kiranmayee Kilaru, Ralph P. Kraft, Tianning Liu, Ryan S. McClelland, Randy L. McEntaffer, Kevin S. McCarley, John A. Mulqueen, Feryal Özel, Giovanni Pareschi, Paul B. Reid, Raul E. Riveros, Mitchell A. Rodriguez, Justin W. Rowe, Timo T. Saha, Mark L. Schattenburg, Andrew R. Schnell, Daniel A. Schwartz, Peter M. Solly, Robert M. Suggs, Steven G. Sutherlin, Douglas A. Swartz, Susan Trolier-McKinstry, James H. Tutt, Alexey Vikhlinin, Julian Walker, Wonsik Yoon, William W. Zhang, "Lynx Mission concept status", Proc. SPIE 10397, UV, X-Ray, and Gamma-Ray Space Instrumentation for Astronomy XX, 103970S (19 September 2017);

(3) Van Speybroeck, L.P.; Jerius, D., Edgar, R. J., Gaetz, T. J., Zhao, P,; Reid, P. B, "Performance expectation versus reality," Proc. SPIE 3113, p. 89–104 (1997).

(4) DeRoo, C.T., Allured, R., Cotroneo, V., Hertz, E., Marquez, V., Reid, P.B., Schwartz, E.D., Vikhlinin, A., Trolier-McKinstry, S., Walker, J., Jackson, T.N., Liu, T., Tendulkar, M., "Deterministic figure correction of piezoelectrically adjustable slumped glass optics," Proc. SPIE, 10399–58 (2017)

(5) Zhang, W.W., Allgood, K.D., Biskach, M.P., Chang, K.-W., Hlinka, M., Kearney, J.D., Mazzarella, J.R., McClelland, R.S., Numata, A., Olsen, L.G., Riveros, R.E., Saha, T.T., Solly, P.M., "Monocrystalline Silicon and the Meta-shell Approach to Building X-ray Astronomical Optics," Proc.SPIE, 10399–27 (2017)

(6) Civitani, M.M., Basso, S., Citterio, O., Holyszko, J., Ghigo, M., Pareschi, G., Parodi, G., Toso, G.Vecchi, G., "Thin fused silica shells for high-resolution and large collecting area x-ray telescopes (like Lynx/XRS)," Proc. SPIE 10399-31 (2017).

(7) Broadway, D. M., Weimer, J., Gurgew, D., Lis, T., Ramsey, B. D., O'Dell, S. L., Gubarev, M., Ames, A., & Bruni, R., "Achieving zero stress in iridium, chromium, and nickel thin films," SPIE9510, 0E15pp (2015).

(8) Chase, R. C.; van Speybroeck, L. P., "Wolter-Schwarzschild telescopes for X-ray astronomy", Applied Optics, Vol. 12, p. 1042 - 1044 (1973)

(9) Claude A. Klein, "Characteristic strength, Weibull modulus, and failure probability of fused silica glass," Optical Engineering 48(11), 113401 (1 November 2009)

(10) L. Proserpio, et al.," Design and development of thin quartz glass WFXT polynomial mirror shells by direct polishing", Proceedings of the SPIE, Volume 7732, article id. 77320D, 14 pp. (2010).

(11) M. Civitani, et al., "Thin glass shell oriented to wide field x-ray telescope", Proceedings of the SPIE, Volume 8443, article id. 84430Q, 13 pp. (2012)

(12) D. D. Walker, et al., "Precessions process for efficient production of aspheric optics for large telescopes and their instrumentation", Proc. SPIE, 4451, 267 (2002)

(13) M. M. Civitani, J. Hołyszko, G. Vecchi, "Probing 3M™ Trizact™ abrasive pads in the polishing and super-polishing phase of Fused Silica", Proc. SPIE 10706, Advances in Optical and Mechanical Technologies for Telescopes and Instrumentation III, 107063K (2018);

(14) Wenin Liao, Yifan Dai, Xuhui Xie, and Lin Zhou, "Morphology evolution of fused silica surface during ion beam figuring of high-slope optical components"Appl. Opt. 52, 3719-3725 (2013)

(15) M. Ghigo, S. Cornelli, R. Canestrari, D. Garegnani, "Development of a large ion beam figuring facility for correction of optics up to 1.7 m diameter" PROC SPIE 7426, 742611 (2009)

(16) M. Ghigo, G. Vecchi, S. Basso, O. Citterio, M. Civitani, E. Mattaini, G. Pareschi, G. Sironi, "Ion figuring of large prototype mirror segments for the E-ELT", Proc. SPIE 9151, (2014)

(17) Vecchi, G., et al., "A bonnet and fuid jet polishing facility for optics fabrication related to the E-ELT," Mem. S.A.It. 86, 408 (2015)